Extension of computer vision algorithms for characterization of coupled interactions between shockwaves and cavitation cloud

Elad Zur

Supervisor: Igal Gluzman

Technion Faculty of Aerospace Engineering

22.03.2024

Table of Contents

Abstract

The complex coupled interactions between nonspherical bubbles in the cavitating clouds and bubbly shocks are extremely challenging to obtain from experimental measurements. It requires the simultaneous monitoring of spatial-temporal evolution shock waves in the cavitation cloud with monitored bubble dynamics. In this report, we have reproduced and expanded the Computer Vision (CV)-based data processing code of [Gluzman and Thomas, 2022a] for bubble detection with new shock-wave detection capabilities from high-speed imaging recordings to obtain valuable data on shock wave morphology evolution and their coupled interactions with nonspherical cavity voids in cavitating flow. For that task, we have utilized the enhanced gradient shadowgraphy technique proposed by [Gluzman and Thomas, 2022b] to detect the presence of shock-waves in aerated cavitating flows, which we couple with our CV code blob analysis procedures to detect and characterize the spatial-temporal evolution of shock-waves simultaneously with bubbles. We first compare and validate our reproduced detection code with experimental results from [Gluzman and Thomas, 2022a] to characterize bubble breakup kinematics only in CD nozzle flow. Then, we validate our method to obtain shock speeds with results reported by [Gluzman and Thomas, 2022b] in aerated cavitating flows in CD-nozzle, and then use our code to obtain new data on shock-wave morphology and coupled interactions with injected bubbles, which understanding is of high importance for the development of new models for predicting the cavitation physics in different liquids.

1. Introduction

The cavitation phenomenon is associated with the process of rupturing a liquid by a pressure decrease below the saturation/vapor pressure threshold, forming cavities/bubbles with gaseous/vaporous content or both. A large number of studies and efforts were devoted to understanding and characterization of different aspects of cavitation [Xing and Frankel, 2002, Coutier-Delgosha et al., 2006, Agarwal et al., 2023] and bubble dynamics [Brenner et al., 2002, Snyder et al., 2007, Zhou and Prosperetti, 2020] behavior in different flow regimes. Understanding the fundamental physical mechanisms of the resulting complex nonspherical bubble dynamics [Salibindla et al., 2020] that may grow or collapse and interact with each other and the associated bubbly shocks [Supponen et al., 2017] is an active research topic and of high importance in many practical applications. However, these complex coupled interactions between nonspherical bubbles in the cavitating clouds and bubbly shocks are extremely challenging for experimental measurements and high-fidelity simulations. It requires monitoring many cavity voids, which expand, split, collapse, and give rise to new cavities in the complex motion of the cavity cloud. Also, it requires the identification of shock waves and monitoring of their spatial-temporal evolution in the cavitation cloud cluster simultaneously with monitored bubble dynamics.

Recent progress has been made, where in [Gluzman and Thomas, 2022a], a novel data processing code was developed that employs advanced Computer Vision (CV) algorithms to extract quantitative data from non-intrusive, time-resolved imaging techniques applied to the bubble spatial-temporal evolution, breakup dynamics, and cavitation inception mechanisms in jet fuels flowing in a stable liquid state inside a CD-nozzle. The CV ”blob” (a term commonly used in image processing applications to describe a region of pixels with some common properties) statistics provided unprecedented quantitative data from non-intrusive imaging technique, revealing valuable new insights into the physics of bubble breakup, nonspherical cavities spatial-temporal evolution, and cavitation inception mechanisms. In [Gluzman and Thomas, 2022b], the authors employed a recently developed enhanced gradient shadowgraphy technique, which allows revealing two-way coupling interactions between the cavities and the associated bubbly shocks in aerated cavitating flow (the cavitation process was controlled with micro-air bubbles injected into the two phase cavitating flow). The technique was used to study the bubbly shock propagation and generation mechanisms in cavitating fuels in CD-nozzle. However, detailed coupled interactions between the bubbles and shocks have not been studied, for which an image analysis technique that is capable of detecting simultaneous spatial-temporal behavior of shock and bubble voids is needed. The current CV code proposed by [Gluzman and Thomas, 2022a] is capable of detecting bubbles but without the ability to detect bubbly shocks and bubbles simultaneously. The ”blob” statistics on these bubble-shock interactions would provide valuable experimental data that would shed light on the complex interactions of bubbly shocks with bubbles in cavitating flows.

The goal of this project is to reproduce and expand the CV-based data processing code of [Gluzman and Thomas, 2022a] with shock-wave detection capabilities to obtain valuable data on shock wave morphology evolution and their coupled interactions with nonspherical cavity voids in cavitating bubbly flow. The motivation of this project is the need for quantitative experimental data on the spatial-temporal behavior of shock-wave and nonspherical cavity voids in internal flows to improve modeling capabilities in predicting the cavitation behavior of different liquids.

In this report, we first discuss the development of our CV code in Section 2, where we first discuss the main functions we used to reproduce the CV detection code of [Gluzman and Thomas, 2022a]. Second, we utilized an enhanced gradient shadowgraphy data processing technique that proposed by [Gluzman and Thomas, 2022b] to isolate bubbly shock waves from experimental data on aerated cavitating flow in [Gluzman and Thomas, 2022b]. Third, we couple our CV detection code with an enhanced gradient shadowgraphy procedure to characterize shockwave speeds and their morphology in aerated cavitating flows in a CD nozzle. In Section 3, we first compare and validate our reproduced detection code with experimental results from [Gluzman and Thomas, 2022a] to characterize bubble breakup kinematics only. Then, we show results for utilizing our extended CV code procedure coupled with enhanced gradient shadowgraphy on experimental data of [Gluzman and Thomas, 2022b] for shock wave detection and characterization in aerated cavitating flows in CD-nozzle. In particular, we use a flow case for JP-5 aviation flow at different nozzle inlet-outlet pressure ratios to first validate our method to obtain shock speeds with results reported by [Gluzman and Thomas, 2022b], and then use our code to obtain new data with our new code capabilities to look on shock-wave morphology and coupled interactions with injected bubbles. Lastly, our conclusions and future directions are discussed in Section 4.

2. Methods

In this section, we present the key MATLAB functions that we used to develop our CV code for reproducing the bubble detection results in Gluzman & Thomas (2022a). In the second part, we utilized an enhanced gradient shadowgraphy data processing technique to isolate bubbly shock waves from experimental data on aerated cavitating flow in Gluzman & Thomas (2022b). In the third part, we couple our CV detection code with an enhanced gradient shadowgraphy procedure to characterize shockwave speeds and their morphology in aerated cavitating flows in a CD nozzle.

2.1 Computer vision detection algorithms

Herein, we discuss the main functions to reproduce the computer vision code used in Gluzman & Thomas (2022a) utilized to extract quantitative data from high-speed imaging of the bubble spatial-temporal evolution, breakup dynamics, and cavitation inception in aviation fuels flowing in a stable liquid state inside the diverging portion of a CD nozzle.
To detect the bubbles in the CD nozzle, we use two main functions, *ForegroundDetector* and *BlobAnalysis*. Both functions can be found in the MATLAB Computer Vision toolbox.

The *ForegroundDetector* is a function that is used to separate the foreground from the background. This function utilizes Gaussian mixture models (GMM) (Stauffer & Grimson, 1999), where the function uses the given amount of training frames and generates an intensity distribution histogram, to which it fits a predefined number of Gaussian modes. The function updates the histograms over time to determine the motion of moving objects and stationary objects, where stationary ones are categorized as part of the background. This function can also be applied to colored videos; however, in our study, we only tested in on grayscale images. The output from this function is a black-and-white image, where the white pixels belong to the foreground and the black to the background.

Several input parameters to the *ForegroundDetector* function can be used to tune the function performance, in particular in determining blob boundaries, which are of high importance in case two blobs are close to each other, where if not properly tuned, the function can merge them and consider it as one blob.

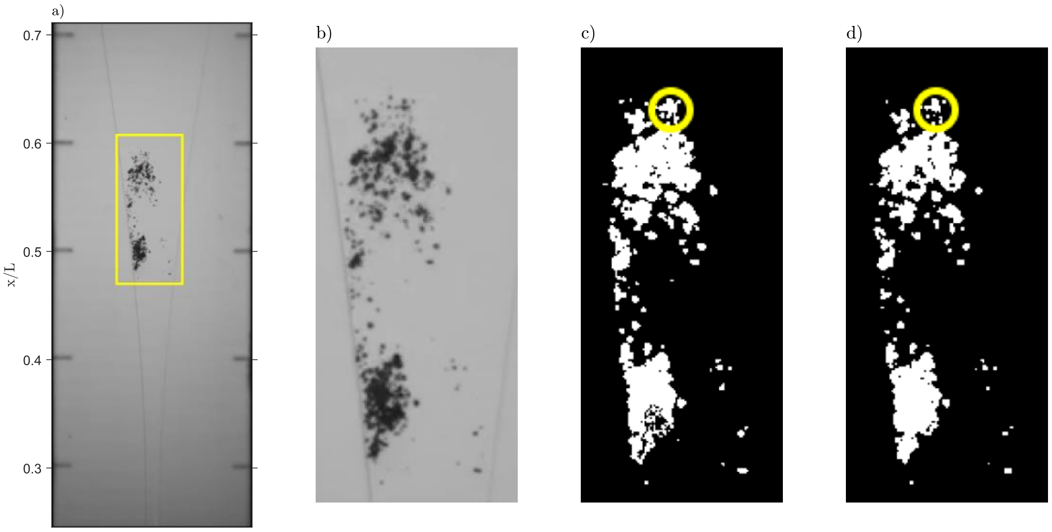

Fig 1 - Example of use of GMM for two different sets of parameters. a) Single frame from Gluzman & Thomas (2022a) experimental data (illustrated for JP-5 fuel at $p_b/p_0 = 0.69$). b) Enlarged region of the image in yellow rectangle that shown in plot a, showing a group of cavities resulting from bubble breakup at the diverging section of the nozzle. c,d: segmented moving cavities from the background via foreground detector based on GMMs for different sets of parameters: Case 1: (K,N) = (3,50) and Case 2 (K,N)=(5,10), respectively.

We illustrate the effect of two of these tuning parameters---K that represents the number of the Gaussian modes, and N that represents the number of training frames---on high-speed imaging data from Gluzman & Thomas (2022a). In Fig. 1a, we show a group of cavities resulting from bubble breakup in the diverging section of the nozzle over for JP-5 fuel at a nozzle pressure ratio $p_b/p_0 = 0.69$, where p_b is the imposed nozzle back pressure and $p_0 = 101.3$ kPa is the inlet nozzle pressure. In Fig. 1b we zoom in on the region within the yellow rectangle of Fig. 1a. In Fig. 1c and Fig. 1d, we show this zoomed region after the application of the *ForegroundDetector* function for two cases: Case 1: (K, N) = (3,50) and Case 2 (K, N)=(5,10), respectively. First, it can be seen from these plots that the nozzle boundaries are recognized as part of the background. Second, theare are slight differences between the plots, which we highlight by the yellow circle. It can be seen that the blobs in the marked area are merged in Fig. 1c, whereas in Fig. 1d, they remain separate.

The second function that we utilize in our CV code is the *BlobAnalysis,* to compute statistics for connected regions in a binary image (Chen et al., 2007) after the application of the *ForegroundDetector* function. In our case, we use this function to extract for each frame the area of each blob, its centroid location and highlight each detected blob by drawing rectangle around it as shown in Fig. 2.

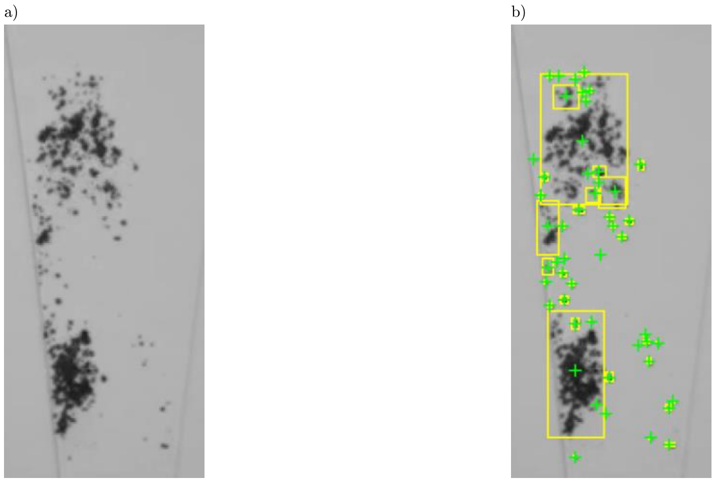

Fig 2 - Example of marking blobs using the BlobAnalysis output. a) Enlarged region of single frame, showing a group of cavities resulting from bubble breakup at the diverging section of the nozzle. b) Each separated blob is framed by a yellow rectangle, and the green (+) symbols denote the blob centroids.

In Fig. 2, we show an example of marking the different blobs in a specific frame with the data collected by the *BlobAnalysis* function. The rectangles mark the borders of each blob, and the cross is the center of each one of them.

In detail, summing the area of all the blobs gives us the total area, $A_{b,tot}$, of the bubbly cloud within the liquid for each time. By combining the data about the blob area and their centroids, we get the center of mass location of the entire bubbly cloud, which location in the vertical direction, x, (the axial direction of the nozzle) is obtained using the next formula,

$$x_{c.g} = \frac{\sum x_i A_i}{A_{tot}}. \tag{1}$$

The centroid location of the bubbly cloud is mainly determined by bigger blobs, which have more impact on the weighted average than smaller blobs.

We save the center of mass location along the video as a vector and apply time differentiation of the vector to yield the velocity and acceleration of the center of mass of the bubbly cluster as follows:

$$v_{c.g} = \dot{x}_{c.g}, \tag{2}$$

$$a_{c.g} = \dot{v}_{c.g} = \ddot{x}_{c.g}. \tag{3}$$

2.2 Enhanced gradient shadowgraphy:

Before utilizing our CV code to detect shockwaves in cavitating flows, we discuss an adaption of an image processing technique denoted as enhanced gradient shadowgraphy and proposed by Gluzman & Thomas 2022b, for enhancing the bubbly shock wave presence in aerated cavitating flows. We study the application of such a technique on a video of aerated cavitating JP-5 at pb/p0=0.25 in CD nozzle, from experimental data of Gluzman & Thomas 2022b, where in addition to the cavitating flows, a stream of bubbles are injected at the nozzle inlet to increase the void fraction, and a raw frame of such flow is shown in Fig. 3. The video we used was in a grayscale form. It means that each frame is represented by a matrix of pixels, while each pixel gets a value between 0 to 1, according to its brightness. The brighter the pixel, the higher its value will be.

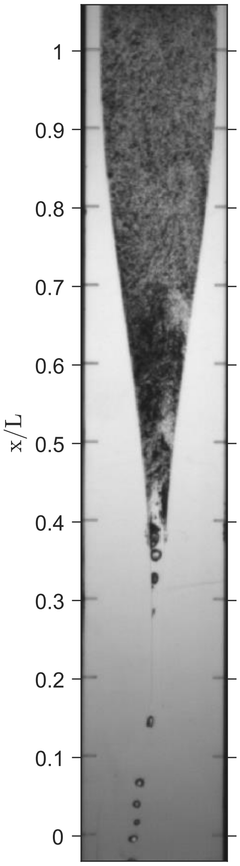

Fig 3 - Raw frame of aerated cavitating JP-5 at pb/p0=0.25. flow obtained via a shadowgraphy imaging in CD-nozzle system setup, using experimental data from (Gluzman & Thomas, 2022b). The nozzle length is $L = 127[mm]$.

The enhanced gradient shadowgraphy method allows us to identify the shockwave presence by identify pixel intensity changes, which are associated to cavities compression and collapse due to shock presence. In this method, a temporal gradient of the recorded frames enhances the pixel intensity changes. A positive change in intensity is defined as an increase in pixel brightness (corresponding to a reduction in void fraction). We obtain this by subtraction from a given frame j, which is the previous one (j-1), as shown in Fig. 4a and Fig. 4b, respectively. The resulting field after subtraction is shown in Fig. 4c.

Our extension technique for utilizing it with our CV code is as follows. We segment the shockwave shape from Fig. 4c by setting a threshold to obtain a binarized image as illustrated in Fig. 4d, where we set this threshold to value 0, which yields a noisy image, which makes the task of the shockwave detection with our CV code much more challenging. Therefore, a filtering procedure for noise removal is applied. Each pixel that gets a value that is greater than zero has been tested with its near surrounding pixels. If the number of positive neighbors was above a certain threshold, we kept that pixel, else we nullified its value, where we found that 10-15 pixels neighboring pixels are sufficient to clear the noise as shown in Fig. 4e. After using our filtering method, we identify two segmented regions

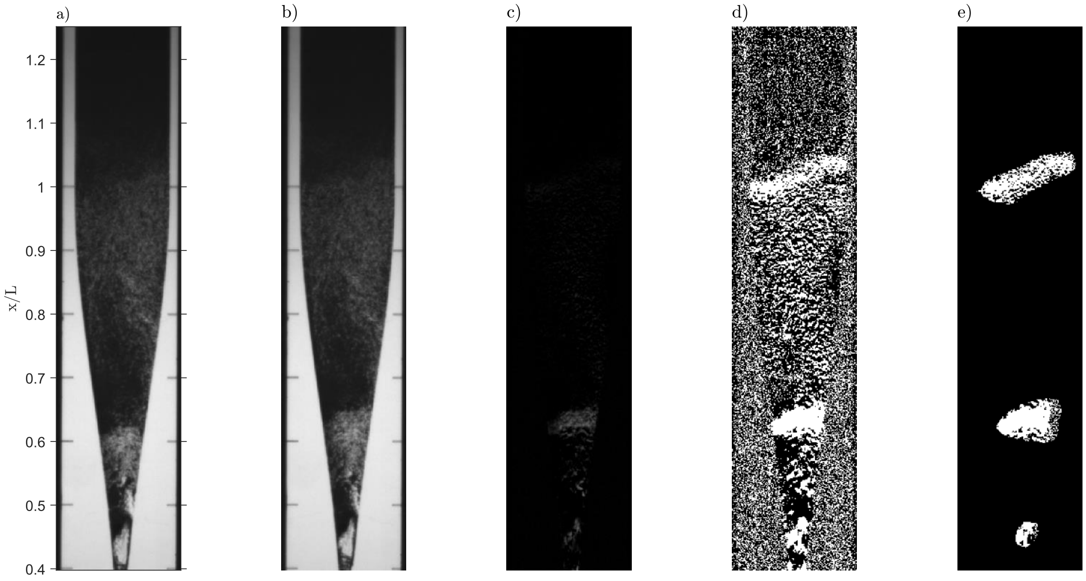

Fig 4 - Example of cleaning the enhance gradient shadowgraphy image. a,b) Two consecutive cropped raw frames showing the diverging part of the nozzle. c) a positive change in pixel intensity (corresponding to an increase in void fraction) by subtraction from a given frame j its previous one, j − 1. d) binary image of c, each white pixel represents a positive change in intensity without importance to the value. e) the remaining pixels after activating the cleaning method on d). They should represent the shock-waves in the nozzle.

that correspond to the shock waves in the flow. We note that the parameter of neighboring pixels and the value of the threshold that we used for filtering is noise is carefully tuned so as not to hinder the shape of the shockwave.

2.3 Coupling CV code with Enhanced Gradient Shadowgraphy:

After the application of enhanced gradient shadowgraphy with our filtering method to obtain binarized videos of shock waves in the high-speed video, we use the *BlobAnalysis* function to obtain the shock waves statics, focusing on the shocks area and their centroids locations. Both are used for studying the shocks spatial-temporal evolution and their shape morphology. In particular, herein, we focused on quantifying the upstream traveling shock-speeds and their shape---external perimeter---variation in CD-nozzle in cavitating aviation fuel. In Fig. 5, we show an example of the obtained shock wave perimeter by our CV algorithm. The result is not perfect. There are parts of the shock wave perimeter that appear to be outside the nozzle boundaries. This imperfection may be solved by fixing our filtering parameter and also testing the regular *ForegroundDetector* for that task, which will be subject to future studies. Still, despite this, the method captures well the leading trailing edges of the shock wave perimeter, which can provide valuable data in studying shock interaction with cavitating flow and other shocks.

Fig 5 -Example of shockwave perimeter detection. a) raw image of divering part of CD nozzle for JP-5 at pb/p0 = 0.25. b) higligited perimeters of the detect bubbly-shocks.

3. Results

This chapter is divided into two subsections: in Subsection 3.1, we validate our reproduced bubble detection code with experimental results from Gluzman & Thomas, (2022a), and in Subsection 3.2, we utilize our extended CV code procedure coupled with enhanced gradient shadowgraphy on Gluzman & Thomas, (2022b) experimental data for shock wave detection and characterization in aerated cavitating flows in CD-nozzle.

3.1 Bubbles Detection

In this section, we compare and validate our reproduced bubble detection code with experimental results from Gluzman & Thomas, (2022a), where we reproduce Figure A.13 for two different parameter settings for the number of Gaussian weights K, and number of training frames, N. In Case 1: $(K, N) = (3,50)$ and Case 2: $(K, N) = (5,10)$. Fig. 6.I shows our result, which we compare with original figure shown in Fig. 6.II. In detail, we used experimental results for a single injected bubble to JP-5 fuel flowing in CD-nozzle with a driven pressure ratio of pb/p0 = 0.69, where the flow did not cavitate and only bubble break was observed in the diverging section of the nozzle. The breakup kinematics, that includes counting the number of detected cavities $N_b(t)$ in Fig 6a; the total area of the cavities at each frame $A_{b,tot}(t)$ in Fig 6b; voids total expansion rate, $\frac{d}{dt}(A_{b,tot}^{1/2}(t))$ in Fig 6c; Center of mass of the detected cavities vertical position, $x_b(t)$ in Fig 6d; center of mass vertical velocity $v_b(t)$ in Fig 6e; and center of mass vertical acceleration $a_b(t)$ in Fig 6f. The breakup time t_d is denoted by a vertical red dashed line in all plots. Comparing Fig. 6.I with Fig.6II shows that our detection code results are strongly similar to results in Gluzman & Thomas, (2022a). However, some discrepancies are observed in the obtained breakup time, which is determined by the minimum of the acceleration curve as shown in Fig. 6f, where our results yield slightly different values for each case, whereas in the original results by Gluzman & Thomas, (2022a) this point is same for both cases. Also, a slight discrepancy is evident in overall number of bubbles (Fig 6a) after breakup and their total area (Fig 6b). In our figure, the number of bubbles is slightly below 60 with an overall area close to 13 mm^2 at 7 ms, whereas in the original data, it is closer to 80 with an overall area closer to 15 mm^2. Overall, we conclude that our solver performs quite well, where these slight discrepancies might be due to a difference in the frames processing of the available recording, such as slightly different cropping areas of the nozzle for bubble detection application. Addressing these slight discrepancies is subject to future investigation.

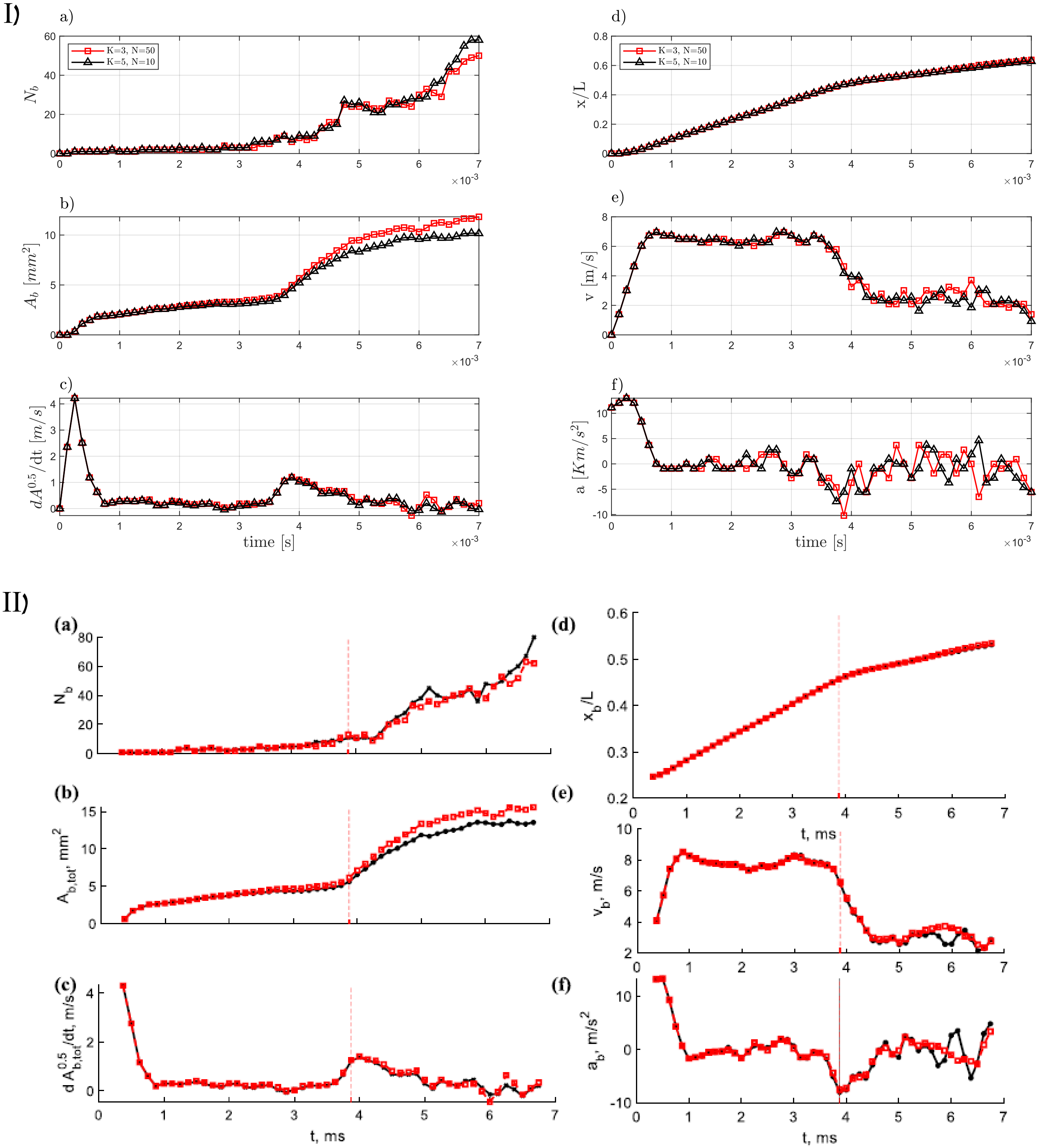

Fig 6- I) our results, II) reprinted from Gluzman Thomas paper. Bubbles detection results. The top figures are our CV detection code application results, and the bottom is the original results reprinted from Gluzman & Thomas, (2022a), Figure A13. (a) Number of detected cavities. (b) Total area of the cavities at each frame. (c) Voids total expansion rate. (d) Center of mass of the detected cavities position. (e) Center of mass velocity. (f) Center of mass acceleration. The breakup time is denoted by vertical dashed line in all plots. Illustrated for JP-5 fuel driven by a nozzle back pressure ratio pb/p0 = 0.69. Case 1: (K,N) = (3,50) (red curve with square symbols) and case 2 (K,N)=(5,10) (black curve with asterisk symbols).

3.2 Shockwave Detection

Herein, our extended CV code procedure is coupled with enhanced gradient shadowgraphy and applied to experimental data of Gluzman & Thomas, (2022b) for shock wave detection aerated cavitating flows in CD-nozzle. In particular, we use a flow case for JP-5 at different pb/p0 with a single bubble injector to first validate our method to obtain shock speeds with results reported by Gluzman & Thomas, (2022b), and then use our code to obtain new data with our new code capabilities to look on shockwave morphology and coupled interactions with injected bubbles.

In Fig. 7, we show our CV tracking procedure to detect upstream traveling shockwave centroid locations for JP-5 at pb/p0 = 0.25 in the diverging part of the CD-nozzle. We note that in this experiment, there was a single bubble injector active (as shown in Fig 3), which triggered the collapse of the attached cavity in the diverging section of the nozzle, and emitting shock that propagated upstream. By fitting linear curves to the identified upstream shockwave events, we obtain the velocity of each detected shock. By averaging the slopes, I get the average shockwave velocity.

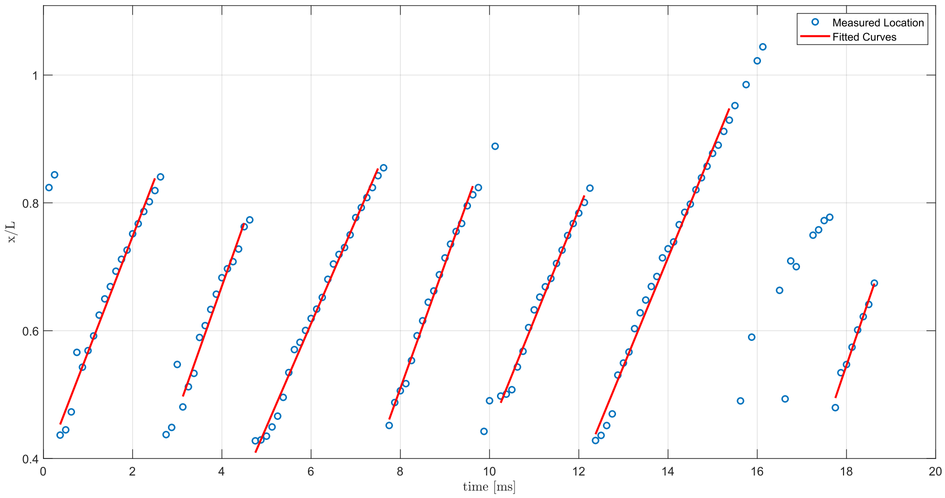

Fig 7- Time history of shockwave location fitted with linear curves for aerated JP-5 at pb/p0 = 0.25. The curve slope correspond to upstream shock propagation velocity in the diverging section of CD-nozzle.

In Fig. 8, we show the tested bubbly shock wave perimeter evolution at three consecutive frames with 0.125 [ms] time differences between the frames, revealing its morphology and interaction with cavitating flow. The complex behavior of the leading and trailing edge of shock shape morphology is subject to detailed study in the future.

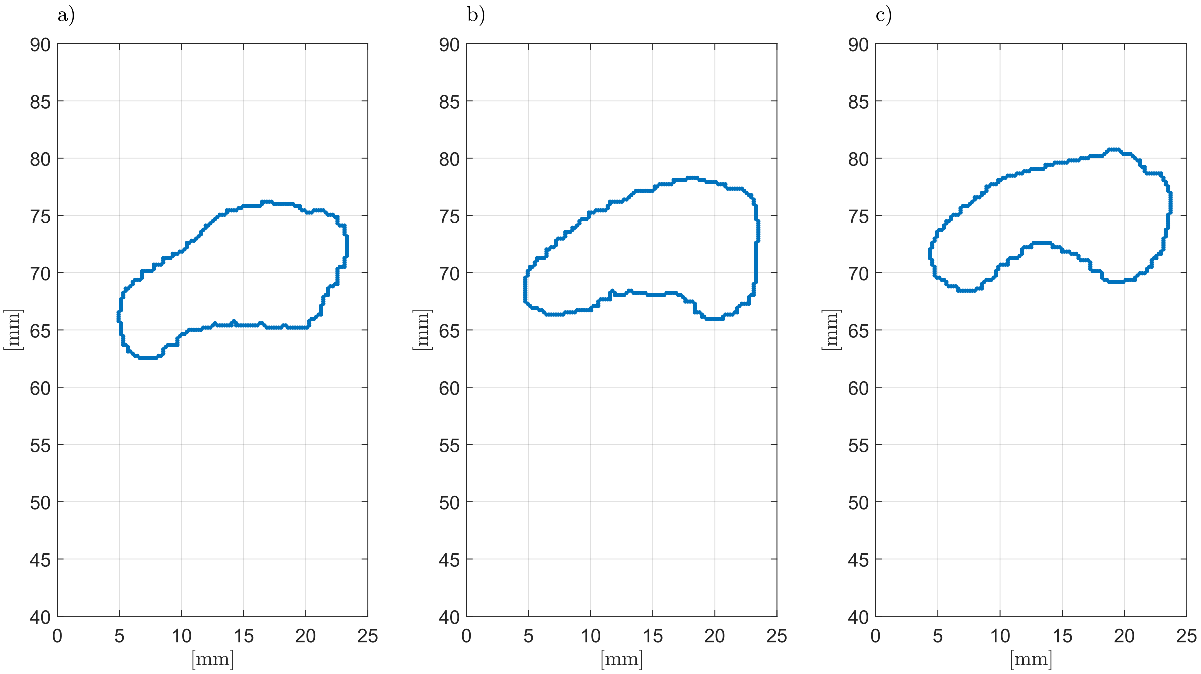

Fig 9 - Single bubbly-shockwave perimeter evolution at three consecutive frames with 0.125 [ms] time differences between the frames. a) refer to the i frame. b) refer to the (i+1) frame. c) refer to the (i+2) frame for aerated JP-5 at pb/p0 = 0.25.

In Fig. 9, we show the application of our extended CV code to study shock speed variation for different inlet-outlet nozzle ratios. We used experimental data recordings of Gluzman and Thomas, (2022b) for aerated cavitating JP-5 flow with a single injector.

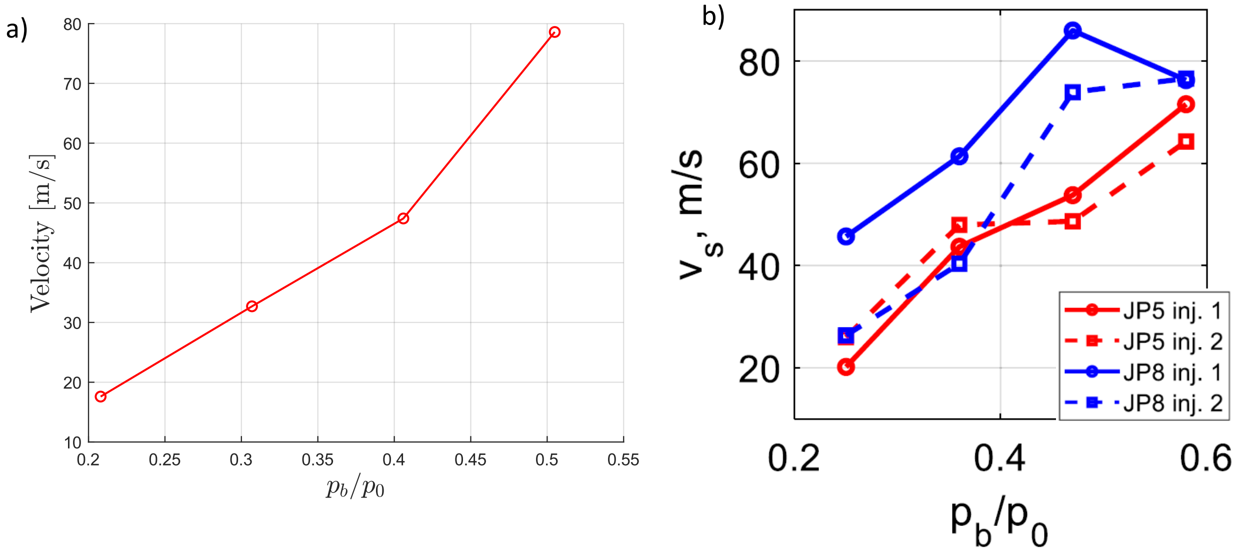

Fig 8- Downstream (upwards) traveling shock wave speed, in range x/L = 0.4–1 for different nozzle inlet-outlet pressure ratios: (a) our code, results for JP-5. Circle marked line is for the results using BlobAnalysis method. Triangle marked line for the results of averaging the pixels. (b) from Figure 9e reprinted from Gluzman and Thomas (2022b), where experiments conducted with JP-5 (red) and JP-8 (blue), using single (solid) and double bubble injectors (dashed).

We validate our results by comparing it with results from Fig. 9 of Gluzman & Thomas, (2022b), which is shown in Fig. 9b, for four different cases: JP8 fuel, JP5 fuel, and single and double injectors. Where we only compared JP5 with a single injector case. One can see that our CV shock detection procedure that used blob analysis performs well with excellent agreement with velocities documented in Gluzman & Thomas, (2022b), with slightly higher values, which were obtained by using other approach based on documenting shocks frontline time history along CD nozzle centerline. In our method, we obtain the entire morphology of the shock, where it is evident that the leading and trailing edges did not move at the same velocity due to shock interaction with the cavitation cloud.

Lastly, we use the benefits of our new CV procedure to detect simultaneously both the spatial-temporal evolution of injected bubbles passing through the nozzle throat and the shocks, which reveal a clear relationship between the two, as shown in Fig. 10.

In Fig. 10, we can see a strong correlation between the total bubbles area while it expends in x/L at 0.1-0.35 nozzle region and the shockwave appearance right after it. In Fig. 10, we can see a pattern of high peaks in the bubble area, which represents the injected bubble explosive growth in that region. Whereas, in Fig. 10b, we show the centroid location of the detected upwards (downstream) shockwave propagation in the diverging section of the nozzle, in x/L between 0.4-1, where the fitted curve slopes correspond to shock speeds. The slopes of the fitted curves look similar, and their frequency appears to be constant with

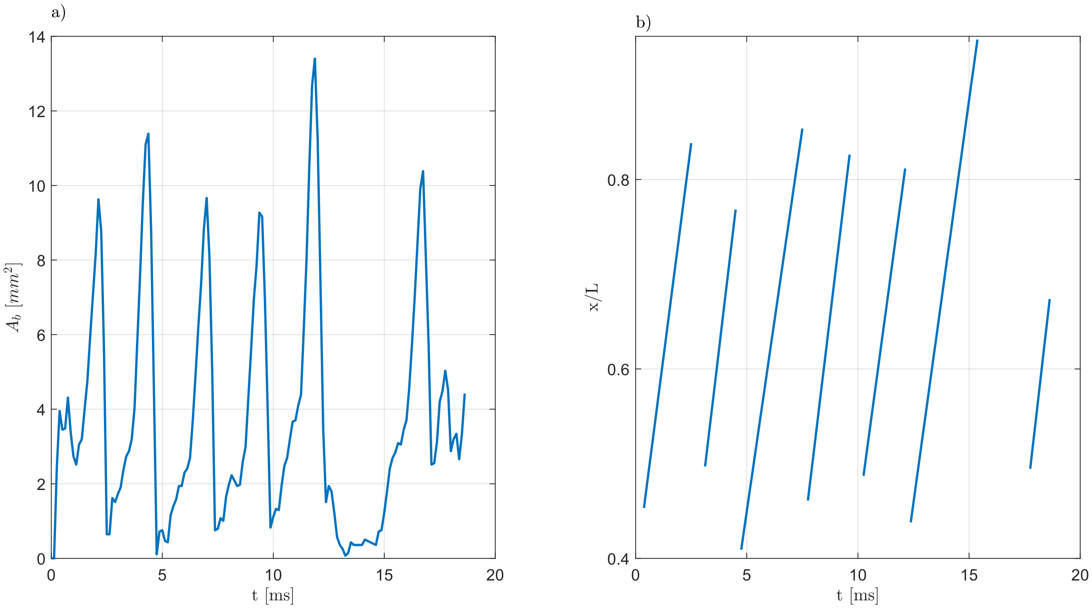

Fig 10 - Coupled results of bubbles detection and shock waves detection, for JP-5 at pb/p0=0.25. a) total area of detected bubbles in x/L at 0.1-0.35. b) time history of bubbly-shock wavefronts detections, represents by the fitted curves, in x/L between 0.4-1.

bubble explosive rate events, indicating that injected bubbles triggered the attached cavity in the diverging section to collapse and emit an upward shock wave. We can recognize six peaks in Fig. 10a and seven shockwaves in Fig. 10b, where the extra shock wave is probably due to injected bubbles before the documented time range.

4. Conclusion and discussion

In this project, we adapted CV methods to develop an image processing procedure for quantifying the spatial-temporal evolution of bubbly shock waves in cavitating flows. In the first part, we used our CV detection procedure to successfully reproduce the results reported in Gluzman and Thomas (2022a) that extracted quantitative data from high-speed imaging on the bubble spatio-temporal evolution in aviation fuels flowing in the CD nozzle. We explored the GMM and Blob analysis methods and learned about the impact of different tunning parameters on detection performance.

In the second part, we coupled our CV detection procedure with an image processing method denoted as the enhanced gradient shadowgraphy method to identify shock waves in aerated CD nozzle flow, using the experimental high-speed imaging data from Gluzman and Thomas (2022b), where bubbly shock wave propagation and generation processes in aviation fuel cavitation are experimentally characterized in a CD nozzle geometry. A noise removal procedure was established to reduce CV code false detections of the shock structures and we demonstrated a successful application of the Blob analysis procedure to extract novel data on bubbly shock morphology, including the varying perimeter of the shocks and the pressure disturbance within its perimeter while its propagation through bubbly cavitating flow domain.

In the last part of our study, we extended our CV code to obtain simultaneous coupled bubble detections with shock detections. By doing this, we demonstrated the connection between the injected bubbles that triggered the attached cavity collapse and the emitted shocks, where we also quantified both bubbles and shock kinematics at once. In future studies, we will utilize our novel code to reveal the complex physics of coupled interactions between bubbly shocks and cavitating bubbly clouds that are shed from the attached cavity in the diverging section of the CD nozzle.

5. References

1. Agarwal, K., Ram, O., Lu, Y., and Katz, J. (2023). On the pressure field, nuclei dynamics and their relation to cavitation inception in a turbulent shear layer. Journal of Fluid Mechanics, 966: A31.
2. Brenner, M. P., Hilgenfeldt, S., and Lohse, D. (2002). Single-bubble sonoluminescence. Rev. Mod. Phys., 74: 425–484.
3. Coutier-Delgosha, O., Devillers, J. F., Pichon, T., Vabre, A., Woo, R., and Legoupil, S. (2006). Internal structure and dynamics of sheet cavitation. Phys. Fluids, 18(1): 017103.
4. Gluzman, I. and Thomas, F. O. (2022a). Characterization of bubble dynamics in the nozzle flow of aviation fuels via computer vision tools. Int. J. Multiph. Flow, page 104133.
5. Gluzman, I. and Thomas, F. O. (2022b). Image-based characterization of the bubbly shock wave generation and evolution in aviation fuel cavitation. Phys. Rev. Fluids, 7(8): 084305.
6. Salibindla, A. K. R., Masuk, A., Tan, S., and Ni, R. (2020). Lift and drag coefficients of deformable bubbles in intense turbulence determined from bubble rise velocity. J. Fluid Mech., 894: A20.
7. Snyder, M. R., Knio, O. M., Katz, J., and Le Maˆıtre, O. P. (2007). Statistical analysis of small bubble dynamics in isotropic turbulence. Phys. Fluids, 19(6): 065108.
8. Supponen, O., Obreschkow, D., Kobel, P., Tinguely, M., Dorsaz, N., and Farhat, M. (2017). Shock waves from nonspherical cavitation bubbles. Physical Review Fluids, 2(9): 093601.
9. Xing, T. and Frankel, S. (2002). Effect of cavitation on vortex dynamics in a submerged laminar jet. AIAA journal, 40(11): 2266–2276.
10. Zhou, G. and Prosperetti, A. (2020). Modelling the thermal behaviour of gas bubbles. J. Fluid Mech., 901: R3.